LANGMUIR Article
Cite This: Langmuir 2018, 34, 8550−8559
pubs.acs.org/Langmuir

Tailored Network Formation in Graphene Oxide Gels

Dorsa Parviz,[†,§] Smit A. Shah,[†] Morgan G. B. Odom,[‡] Wanmei Sun,[†] Jodie L. Lutkenhaus,[†,‡] and Micah J. Green*[,†,‡]

[†]Artie McFerrin Department of Chemical Engineering and [‡]Department of Materials Science and Engineering, Texas A&M University, College Station, Texas 77843, United States

Supporting Information

ABSTRACT: Graphene oxide (GO)-based gels are attractive because of their ability to retain individual nanosheet properties in a three-dimensional (3D) bulk material. The final morphology and properties of these 3D gel networks depend strongly on the type and density of cross-links, and these gels can be dried and annealed to form aerogels with both high conductivity (560 S/m) and high surface area (1700 m^2/g). The results show that both ammonia content and the parent nanosheet morphology (crumpled vs flat) have a strong influence on the cross-linked structure and composition; notably, nitrogen is found in the gels, suggesting that ammonia actively participates in the reaction rather than as a mere catalyst. The GO nanosheet morphology may be altered using spray-drying to obtain crumpled GO (cGO) nanosheets and form cGO gels; this allows for an additional handle in the creation of GO-based gels with tunable density, electrical conductivity, and surface area.

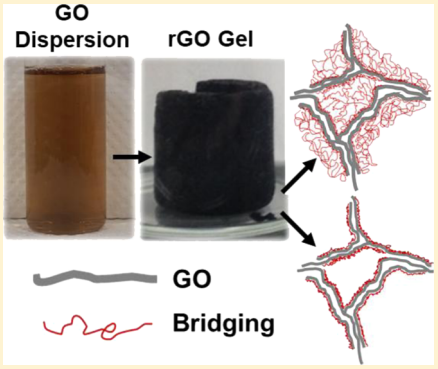

INTRODUCTION

Three-dimensional (3D) graphene networks allow for individual nanosheet properties to be utilized in bulk macroscopic materials while retaining high specific surface area.[1] These 3D networks may be prepared by cross-linking of the two-dimensional (2D) graphene or graphene oxide (GO) nanosheets. These structures are prized for their high electrical conductivity, mechanical strength, and high surface area, making them potential candidates for binder-free electrochemical energy storage with mechanical integrity.[2−4] However, these properties are highly dependent on the nature of the networks' cross-links and processing approach. For instance, the bulk electrical and mechanical responses are dictated largely by the nature of the nanosheet cross-links rather than the individual nanosheet properties.[5] Similarly, the bulk electrochemical or catalytic properties of these materials are limited by features such as pore size distribution and available surface area,[6] which stem not only from precursor nanosheet dimensions but also from the processing technique.

Various techniques have been employed to create graphene-based gels and foams. Pristine graphene 3D structures have been prepared by template-directed assembly of the individual nanosheets.[2,7,8] Alternatively, simple freeze-casting of GO or reduced GO dispersions may form cross-linked porous structures with ice crystals as template.[9] For these techniques, the pore size distribution and surface area are determined chiefly by the morphology of the template itself.[10] Moreover, the removal of the template may be costly and difficult, involving etching solutions or high temperature.[11,12]

GO's versatile surface chemistry allows for a number of additional liquid-phase assembly techniques to prepare 3D networks with no need for templates and/or additives.[13−17] This is typically accomplished through simultaneous partial reduction of GO and cross-linking in aqueous solution to produce a monolithic hydrogel.[18−20] Xu et al. first reported the production of GO hydrogels and their processing into aerogels using a hydrothermal method at high temperatures (180 °C).[19] In a hydrothermal reactor, as the pressure and temperate rise, the solubility of the GO nanosheets and their colloidal stability in the solvent (water in this case) decrease substantially, and they tend to aggregate. When appropriate temperatures and concentrations of GO nanosheets are chosen, the loss of colloidal stability and the reduction of nanosheets occur gradually; thus, controlled cross-linking of the nanosheets takes place rather than aggregation and sedimentation. This leads to formation of a partially reduced GO hydrogel over time. These hydrogels can be converted into a porous, interconnected aerogel structure using either freeze-drying or critical point drying (CPD).[21−23] Further thermal reduction can remove many of the remaining functional groups to yield a conductive reduced GO 3D network.[24] Later, Worsley et al. introduced an alternative hydrothermal method, termed as sol−gel technique, in which ammonia was added to GO dispersions to facilitate the cross-linking of the nanosheets in alkaline media at lower temperatures (80−100 °C).[24] Ever since, various modifications of the hydrothermal approach have been applied to tailor the morphology and properties of graphene-based 3D networks. The lack of additives or templates is a strong advantage of this simple family of techniques.

Received: February 25, 2018
Revised: June 13, 2018
Published: June 28, 2018

DOI: 10.1021/acs.langmuir.8b00637
Langmuir 2018, 34, 8550−8559

However, very few studies have investigated the composition and type of graphene−graphene cross-links created during the GO assembly process in the liquid phase. Xu et al. speculated that cross-linking is mainly caused by the $\pi-\pi$ stacking of the partially reduced GO nanosheets.[19] In another study, Hu et al. investigated the chemical reaction pathways of the GO nanosheet network formation in acidic and alkaline media and proposed various chemical routes for this process.[25] Han et al. showed that GO hydrogels can be treated with ammonia solution to induce formation of covalent cross-links to enhance the gel's mechanical strength.[26] The role of ammonia in nanosheet assembly has not been fully understood in previous studies. Most studies have reported that the sole role of adding ammonia is to make the reaction conditions alkaline.[24,25]

Another factor that has not been examined is the possibility of using crumpled GO (cGO).[27] The use of spherical graphene structures such as cGO rather than native GO would allow for an additional handle in the creation of GO-based gels with tunable density. In our prior paper, we demonstrated that cGO particles can be easily created using spray-drying.[28] Interestingly, redispersion of the aggregation-resistant cGO particles into water preserved the spherical, crumple morphology. The crumpled morphology is preserved because of plastic deformation and possible covalent cross-link formation during the spray-drying process.

In this investigation, we establish synthesis−structure−properties relationships for graphene gelation reactions. We vary the parameters that affect the GO assembly process (e.g., ammonia composition and nanosheet morphology) and analyze the morphological and compositional properties of the products to establish a fundamental understanding of the underlying mechanism. First, we alter the ratio of GO/ammonia to reveal its significant role in formation of the intersheet bridging structures and contribution to the deoxygenation and reduction of the nanosheets as they assemble to form a hydrogel. Second, we investigate nanosheet assembly and aerogel formation using 3D cGO nanosheets instead of native flat nanosheets. We create gels with varying ratios of cGO/GO content in the precursors to study the effects on the morphology, the pore distribution, the electrical conductivity, and surface area of the final aerogel products. Our observations can shed light on the liquid-phase GO assembly mechanism and allow us to tune the morphology and composition of GO gels for future applications.

MATERIALS AND METHODS

Materials. Single-layer GO was purchased from Cheap Tubes, Inc. Aqueous ammonium hydroxide solution [28.0−30.0% (v/v)] was purchased from Sigma-Aldrich. All chemicals were used as received.

Preparation of cGO. To prepare cGO dispersions, GO powder was added to deionized (DI) water to obtain a dispersion with 1 mg/mL concentration and tip-sonicated for 5−10 min. The dispersions were diluted to yield 0.1 mg/mL concentration. The GO dispersions were then processed in a spray dryer (Buchi 290 mini spray dryer) to yield crumpled nanosheets according to the procedure reported in our previous study.[28] The GO dispersion is converted to micron-sized droplets by an atomizer. These droplets are carried through a drying chamber by a concurrent hot air stream. The GO nanosheets are crumpled because of the capillary forces exerted by the drying droplet. These dried cGO flakes are collected in a cyclone separator, and the carrier air is discharged from the separator. Two different batches of cGO particles were prepared by spraying at 120 and 150 °C. In all experiments, 10% of the maximum dispersion flow rate, 40 psi of nozzle air pressure, and 100% of the aspirator rate were used for spraying the dispersions.

Preparation of GO, cGO, and cGO/GO Hydrogels. To prepare 100% GO hydrogels, GO nanosheets were dispersed in DI water with a concentration of 10 mg/mL by 15 min of tip sonication, followed by 1 h of bath sonication. Various amounts of ammonium hydroxide (NH_4OH) (1.8 or 3.6 mL) were added to the dispersions, the mixtures were sealed in glass vials, and placed in an oven at 90 °C. The reaction was carried out for 72 h for the hydrogels to form. GO hydrogels with NH_4OH/GO ratios (v/w) of 0.024 and 0.012 mL/mg were obtained and referred to as high ammonia/GO (HAGO) gel and low ammonia/GO (LAGO) gel, respectively. To prepare 100% cGO hydrogels, cGO particles were added to DI water with 10 mg/mL concentration and bath-sonicated for 2 h to obtain homogeneous cGO dispersions. NH_4OH (3.6 mL) solution was added to the dispersions; the mixtures were sealed in glass vials and placed in an oven at 90 °C. The reaction was carried out for 72 h for the hydrogels to form. To prepare cGO/GO hydrogels, 10 mg/mL of GO and 10 mg/mL of cGO were dispersed in DI water separately using a procedure similar to GO and cGO dispersions. The two dispersions were then mixed to yield solutions with 25, 50, and 75% of cGO total solid mass. The gelation process was similar to that used for 100% cGO gels. Once the gelation process was complete, hydrogels were washed with fresh DI water to remove excess ammonia and reaction byproducts.

CPD of Hydrogels. Before drying, the hydrogels were solvent-exchanged in an ethanol bath for 3 days to remove the DI water. The CPD of the hydrogels was carried out in a Samdri-PVT-3D critical point dryer after solvent exchange with the liquid CO_2 in the dryer chamber. (CPD is useful for removing water without a first-order phase transition; this prevents capillary-induced densification of gels and preserves their mechanical integrity during the drying process.)

Scanning Electron Microscopy. All the aerogels were cut into smaller pieces, and the inner surfaces of the aerogels were mounted on double-sided carbon tape. An accelerating voltage of 2 kV was used to image the top surface and cross section of the samples with a JEOL JSM-7500F instrument.

Thermogravimetric Analysis. Thermogravimetric analysis (TGA) was performed in a TA Instruments Q50 TGA to determine the mass loss of the aerogels. Each sample (30 mg) was heated up from room temperature to 1000 °C at a rate of 1 °C/min in an inert nitrogen atmosphere.

Conductivity Measurements. The electrical resistance of the dried aerogels was measured using the four-point probe method. The four-point probe head (Signatone, SP4-40045TBY) was mounted on a resistivity measurement stand (Signatone, model 302). The spacing between the probe tips was 1.5875 mm. Current was passed to the sample through the outer probes using a Keithley 6221 direct current (dc) source. A Keithley 2000 multimeter was used to measure the voltage across the sample. The sheet resistance and electrical conductivity of the samples were calculated using the measured values of the voltage.

X-ray Photoelectron Spectroscopy. An Omicron X-ray photoelectron spectroscopy (XPS) system with an Mg X-ray source was used for performing XPS measurements. CasaXPS software (version 2.3.16) was used to perform deconvolution. All the aerogels were cut into small pieces and degassed for 48 h prior to the XPS measurements.

Raman Spectroscopy. The Raman spectra were obtained using a HORIBA Jobin-Yvon LabRam HR Raman confocal microscope with 1800 gr/mm gratings for excitation lasers with wavelength of 633 nm. All aerogels were smashed to fine powder and mounted on a glass slide using a double-sided tape for Raman measurements.

Fourier Transform Infrared Spectroscopy. Samples of hydrogels were collected at specific time intervals during the gelation reaction, and the reaction was immediately quenched by placing the samples in an ice bath. These samples were then washed with DI water and ethanol to remove the excessive unreacted ammonia and were casted on a silicon wafer to dry at room temperature for 2 h. These samples mounted on the silicon wafer were then used to collect the Fourier transform infrared (FTIR) spectra using a Thermo Scientific Nicolet IR100 FT-IR instrument.

DOI: 10.1021/acs.langmuir.8b00637
Langmuir 2018, 34, 8550−8559

Brunauer–Emmett–Teller Surface Area Measurements. The surface area of the dried aerogels was calculated through the Brunauer–Emmett–Teller (BET) method from the nitrogen adsorption/desorption isotherms. All the samples were degassed for 24 h prior to the measurements to remove the moisture from their surface. The adsorption of nitrogen was performed at a relative pressure (P/P_0) range of 0.05–0.3.

Electrochemical Characterization of Gels Made Using In-House GO Nanosheets. GO nanosheets were made using a modified Hummer's method.[29] As-obtained GO slurry was bath-sonicated at 55 °C overnight, followed by centrifugation at 2000 rpm for 20 min to separate out the larger flakes. The supernatant was freeze-dried and processed into HAGO hydrogels. As-prepared HAGO hydrogels were washed with water to remove excess ammonia and reaction byproducts. Washed HAGO hydrogels were cut into ~2 mm thick cylindrical slices using a blade. These slices were pressed between aluminum foil sheets using a mechanical press at 500 psi for 1 min, with a 100 μm thick aluminum shim, to obtain a thin hydrogel film. Electrodes with diameters of 3/8″ were punched from the pressed films and used in a symmetric two-electrode supercapacitor cell assembly. Cyclic voltammetry (CV) was carried out in 1M aqueous H_2SO_4 electrolyte from 0 to 0.9 V. A layer of the Celgard membrane was used as a separator. The areal capacitance was calculated from the CV curves using the formula $C = \int_{V_{min}}^{V_{max}} I\, dV/(v \times \Delta V \times A)$, where V_{max} and V_{min} represent the high and low voltage cutoffs (V), respectively, I represents the current (A), V is the applied potential (V), v indicates the scan rate (mV/s), and A represents the nominal area of the electrode (cm^2).

RESULTS AND DISCUSSION

Nanosheet Assembly. A low-temperature sol–gel technique was used to prepare the GO hydrogels according to previously reported procedures.[24] Briefly, a homogenous aqueous dispersion of GO nanosheets at a specific concentration was prepared (Figure 1). Then, ammonia was added to

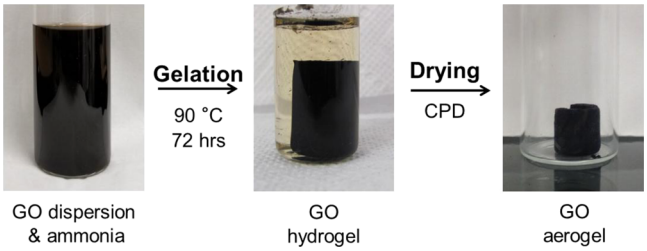

Figure 1. Procedure for preparation of GO aerogels. An aqueous dispersion of GO (1 wt %) and ammonia was reduced in an oven at 90 °C for 72 h. This led to the formation of a dark brown GO hydrogel; CPD was then used to obtain a GO aerogel.

the dispersion and the gelation reaction was carried out for 72 h at 90 °C to form a monolithic GO hydrogel. The color changed from brown in the dispersion to dark brown in the hydrogel, which is indicative of the partial reduction of the GO nanosheets. The hydrogel was washed with DI water to remove the excess ammonia. To avoid shrinkage and collapse of the pores of the hydrogel, it was dried using CPD. The resulting aerogels had a smaller volume than the hydrogels.

To monitor the changes in the surface chemistry of the GO nanosheets during the gelation reaction, we performed FTIR spectroscopy on the samples collected at various stages of gelation (Figure 2). After 12 h of gelation, no visible change in the FTIR spectra of the hydrogels was observed, confirming the completion of the gelation reaction. In the spectra of the original GO nanosheets, we observed a broad peak from 3600

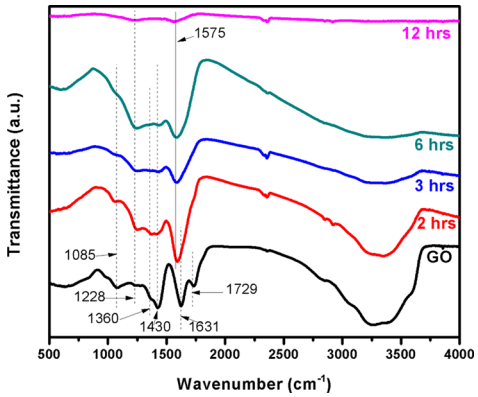

Figure 2. FTIR spectra of samples collected at various stages of the gelation process (up to 12 h of gelation). The peaks of interest are noted.

to 2500 cm^{-1} (O–H bonds), a peak at 1729 cm^{-1} (C═O in carboxyl and ketones) and a sharp peak at 1631 cm^{-1} (adsorbed H_2O). In the fingerprint region of the spectra, we observed a peak at 1430 cm^{-1} (O–H bonds), a peak at 1360 cm^{-1} (C–OH bonds), a peak at 1228 cm^{-1} (S═O impurities), and a peak at 1085 cm^{-1} (possibly because of the epoxide groups). These sulfur impurities stem from sulfuric acid used during the modified Hummer's method for GO synthesis.[30] After 12 h of gelation, only the S═O peak (sulfur impurities) remained in the spectra. This observation verifies the deoxygenation of the nanosheets during the gelation process. However, no new peak appeared in the hydrogel spectra after 12 h, except for a weak and broad one at 1575 cm^{-1}. This peak may be attributed to C–N bonds. (Alternatively, this peak could be attributed to the C═C bonds in the sp^2 network of nanosheets that has been slightly shifted from its characteristic position at 1560 cm^{-1} although such a peak is typically too weak to be detected.) The disappearance of the main peaks of the functional groups in the first couple of hours of gelation indicates that the deoxygenation on the surface of nanosheets occurs quickly. The possible C–N peak appears later in the process, which means that oxygen replacement by nitrogen on the nanosheet surface follows the deoxygenation reactions. This peak becomes weaker throughout the process, possibly indicating the gradual removal of the substituting nitrogen from the nanosheet surface.

Ammonia Effects on Nanosheet Assembly. The role of ammonia in the low-temperature sol–gel preparation of GO aerogels has not been well studied and/or understood. Prior studies used ammonia to adjust the pH of the reaction medium and facilitate the reduction of the GO nanosheets.[24,25] We suggest that the ammonia plays a more significant role in the gel formation process, and alteration of the ammonia/GO ratio affects the morphology, composition, and properties of these aerogels. To examine our hypothesis, we prepared two types of GO hydrogels, LAGO and HAGO. The fractional volume shrinkage during synthesis of LAGO and HAGO hydrogels was calculated to be 71.1 and 71.9%, respectively. Scanning electron microscopy (SEM) images in Figure 3a,c suggest that these two ammonia/GO ratios yield two different morphologies in the final aerogels. The LAGO has a loosely packed structure with thick stacks of nanosheets, whereas the HAGO has a more compact structure in which the sheet-like morphology is not prominent. Both samples contain two

DOI: 10.1021/acs.langmuir.8b00637
Langmuir 2018, 34, 8550–8559

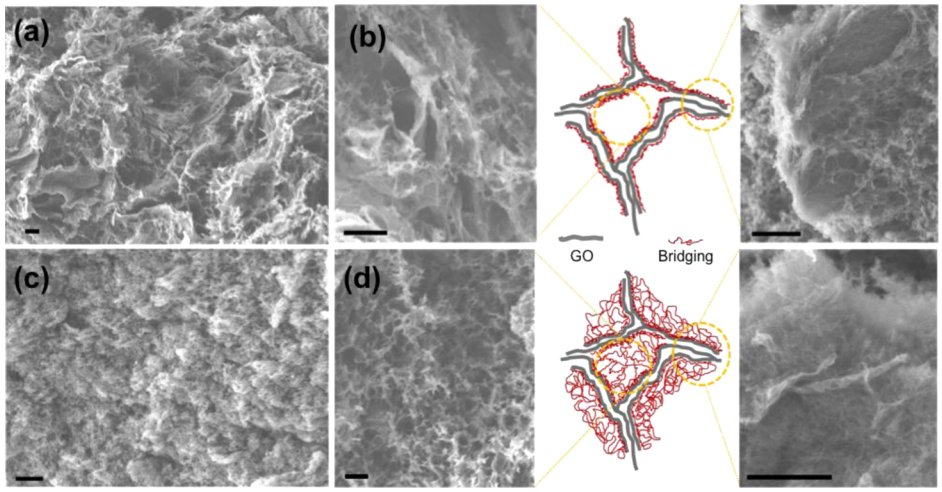

Figure 3. SEM images of (a) LAGO, prepared at an ammonia/GO ratio of 0.012, and (c) HAGO, prepared at an ammonia/GO ratio of 0.024, and proposed mechanism for nanosheets' assembly and bridge formation: (b) LAGO ratio (0.012), (d) HAGO ratio (0.024), (scale bars ∼1 μm in SEM images).

distinct morphological features: (i) large few-micron nanosheets and nanosheet stacks and (ii) smaller (less than a micron) connected web-like species. Moreover, pores in both samples can be distinguished as submicron- and few-micron-sized pores formed by nanosheets, and submicron-sized pores formed because of web-like species. The main difference between the two samples is the presence of more web-like species on the surface of the HAGO sample. We call these species "bridging" structures as they seem to be present in the space between the nanosheets, connecting them to each other. These "bridging" structures are ubiquitous in our SEM images, but there has been little discussion on this topic in the prior literature.[18,20,31,32]

Figure 3b,d shows the porous structure of LAGO and HAGO samples at higher magnifications. In the LAGO, large connected nanosheet structures form the backbone of the 3D structure. A magnified SEM micrograph of an individual stack of nanosheets shows that the bridging structures are mainly present on the surface of the nanosheet stacks. In this sample, bridging structures play a minimal role in filling the pores between the nanosheet stacks. In contrast, in the HAGO, the bridging structures are the dominant features of the morphology and cover the entire sample such that the main backbone of the 3D structure can hardly be recognized. However, trace nanosheet stacks visible in the micrographs indicate that they still form the backbone of the 3D structure in this sample. The pores of this HAGO sample are mainly composed of the spaces between the bridging structures and are much smaller compared to those of the LAGO. This sharp difference in the morphology of the two samples indicates that the GO nanosheets undergo different gelation and cross-linking routes in the presence of varying amounts of ammonia; a higher ratio of ammonia/GO yields more bridging between the nanosheets.

We suggest that the bridging structures present in HAGO and LAGO may be composed of small carbonaceous fragments formed at various stages of the sample preparation and processing. First, the GO synthesis through Hummer's method produces large quantities of highly oxidized carbonaceous debris that adsorb onto the larger nanosheets' surface.[33,34] These small oxidative debris (OD) are highly soluble in a basic aqueous environment because of their large negative surface charge density. In the presence of an excessive amount of ammonia, the OD desorb from the nanosheets' surface and dissolve in water to form ammonium salt.[35] Additionally, it has been demonstrated that the sonication of nanosheets causes fragmentation and produces dispersions with broad nanosheets' size distribution, ranging from a few nanometers to a few microns.[36] Lastly, these small fragments may be produced through GO reduction and cleavage of C−C bonds close close to the edges of larger GO nanosheets.[25] During the gelation process, a large portion of these oxidized fragments become trapped between the larger nanosheets as they undergo deoxygenation and aggregation. Similar to GO nanosheets, the deoxygenation and/or nitrogen replacement of these small fragments leads to covalent and noncovalent bond formation between them and produces an interwoven network that appears as bridging structures in the SEM images. The energy-dispersive spectroscopy (EDS) mapping of the aerogels (Supporting Information section S1) indicated a homogenous distribution of carbon, oxygen, and nitrogen all over the sample surface, confirming that the bridging structures and the larger nanosheets' stack contain similar atomic components. It is noteworthy that similar structures have not been observed in prior GO hydrogel literature (except when GO nanoplatelets with an extremely small platelet diameter were used)[37] because the minimal amount of ammonia used in these studies for adjustment of the solution pH is not sufficient for desorption and detachment of all ODs from the nanosheets' surface.

Both LAGO and HAGO aerogel samples were annealed using a tube furnace in an argon atmosphere at 1050 °C to assess their morphological and compositional changes upon thermal reduction. The SEM images in the Supporting Information section S2 show that the bridging structures may become the dominant morphological feature in both samples after the thermal treatment. This implies that thermal deoxygenation and reduction of these aerogels activates the deoxygenation and cross-linking of the residual nonreacted carbonaceous fragments in both samples. As these fragments are less stiff compared to GO nanosheets, they can deform more easily to facilitate the cross-linking and form a hierarchical, spatially varying network. At 1050 °C, most of these fragments are thermally reduced and cross-linked, and

DOI: 10.1021/acs.langmuir.8b00637
Langmuir 2018, 34, 8550−8559

thus, both HAGO and LAGO show similar morphologies, populated with bridging structures at the surface.

Raman spectra of LAGO and HAGO samples before and after thermal reduction are illustrated in Figure 4. All the

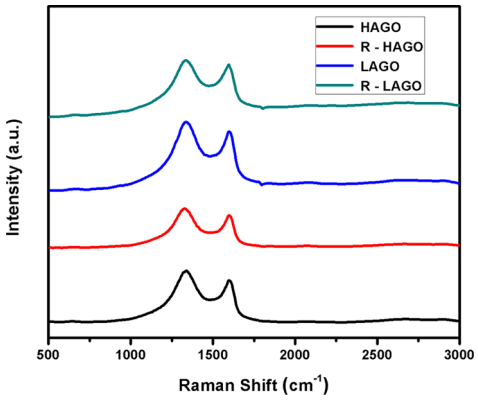

Figure 4. Raman spectra of HAGO and LAGO aerogels before and after reduction.

aerogels have D and G characteristic peaks at 1340 and 1580 cm^{-1}, which are indicative of the structural disorder and the graphitic sp^2-hybridized network of carbon atoms, respectively. Similar to the reported Raman spectra of GO nanosheets,[38] the D peak is sharper than the G peak in both HAGO and LAGO. This implies that despite the deoxygenation of the nanosheets, the sp^2 network recovery is minimal during the gel formation and is consistent with the data reported for reduced GO nanosheets.[39] After the thermal treatment of these samples, the D peak broadens and becomes weaker but still remains sharper than the G peak. The decrease in the D to G peak intensity ratio (I_D/I_G) for both samples implies further sp^2 network recovery upon thermal annealing of the hydrogels; however, residual functional groups and lattice defects are present in both aerogels. Moreover, the 2D peak (2500−2800 cm^{-1}) intensity is almost zero in all samples.

To investigate the effect of the ammonia/GO ratio on the chemical composition of the aerogels, we performed XPS studies on HAGO and LAGO samples. Figure 5a shows survey spectra for the precursor GO nanosheets, HAGO and LAGO samples before and after thermal reduction. HAGO and LAGO spectra show peaks for carbon, nitrogen, and oxygen before thermal annealing. In the C1s XPS spectra of both samples, before annealing (Figure 5c,d), five main peaks corresponding to the sp^2-hybridized C−C bonds, sp^3 C−C, C−O in epoxide, C═O of ketone, and O−C═O in carboxyl groups of the GO were observed at 284.8, 285.6, 286.5, 288.1, and 289.1 eV, respectively. The comparison (Table 1) of the atomic ratio of these samples with the original GO nanosheets (Figure 5b) confirms the deoxygenation of functional groups in both samples. Moreover, a C−N peak at 285.9 eV was observed in both samples, confirming the incorporation of nitrogen from ammonia during the gelation and reduction process. It is important to note that the proximity between C−N (285.9 eV) and sp^3 C−C (285.6 eV) peaks makes it difficult to distinguish between them and may result in uncertainty in the intensity ratio of the components. The N/C atomic ratios in HAGO and LAGO were calculated to be 0.14 and 0.07, respectively, indicating significantly higher nitrogen substitution in the case of HAGO. A comparison of the C−N and C−O peaks in both these samples indicates that a stronger C−N peak is correlated with a weaker C−O peak, possibly indicating that nitrogen substitution occurs through epoxide ring−opening reactions and subsequent nitrogen substitution on the GO surface. N1s spectra of LAGO and HAGO samples (Supporting Information section S3) can be deconvoluted into three nitrogen bonding configurations: pyridinic N (398.0 eV), pyrrolic N (399.8 eV), and quaternary amine (401.2 eV).[40,41] These results are very interesting for applications involving N atom doping in graphene nanosheets.[42,43] Figure 5e,f shows the C1s XPS spectra of the aerogels after annealing. In both the cases, the C−N peak disappears, implying the removal of nitrogen atoms from the nanosheet surface (additional discussion can be found in the Supporting Information section S4). The atomic ratio of elements in the annealed aerogels (Table 1) indicates a similar chemical composition for both sample types, which is consistent with the similar morphological features observed in the SEM images (Supporting Information section S2) and the decrease in the (I_D/I_G) ratio in Raman spectra of both samples (Figure 4).

Moreover, TGA of both LAGO and HAGO samples indicated that these GO aerogels were more thermally stable than the original GO nanosheets, as shown in the Supporting Information section S5. As the temperature was ramped to 900 °C, the mass loss in the original nanosheets (∼65%) was significantly higher than the mass loss in both aerogels (∼35%). This observation confirms that the GO nanosheets have been partially deoxygenated and reduced during the gelation process. (Note: the mass loss during the temperature range of 25−120 °C is likely due to adsorbed water loss; this also accounts for the gap between the HAGO and LAGO trends at higher temperatures.) The significant mass loss in the GO sample at 180 °C can be correlated with the lower C/O ratio in the GO sample (2.3:1) compared to that of LAGO (6.1:1) and HAGO (4.2:1) samples measured using XPS. It is challenging to directly correlate the GO sample's weight loss during TGA with HAGO and LAGO samples' C/O ratio. Unlike the thermally reduced GO sample, LAGO and HAGO samples have carbonaceous bridging structures and cross-links which are formed during the sol−gel process. These cross-links and bridging structures also contribute to the high C/O ratio in HAGO and LAGO samples.

The surface area, density, and conductivity of LAGO and HAGO are listed in Table 2; note that these properties determine functional performance in applied materials such as electrodes or composites. The density of LAGO samples was calculated to be higher than that of HAGO, in contrast to their appearance in SEM micrographs. This implies thicker pore walls in LAGO, which may have formed upon the reduction and $\pi-\pi$ interactions of the reduced GO nanosheets, whereas the bridging structures in HAGO prevented extensive $\pi-\pi$ stacking and densification. Hu et al. saw the same inverse trend between density and ammonia content.[25] Note that they also argued that thicker pore walls result in higher electrical conductivity, whereas we observed comparable values between the two cases. As expected, electrical conductivity values of LAGO and HAGO samples increase drastically upon annealing because of further reduction and restoration of the sp^2 network. Consistent with the observed HAGO morphology, the HAGO samples possess higher BET surface area compared to LAGO. These surface area data imply that the increased bridging structures in the aerogels prepared with a higher ammonia/GO ratio increase the available surface area of the samples.

DOI: 10.1021/acs.langmuir.8b00637
Langmuir 2018, 34, 8550−8559

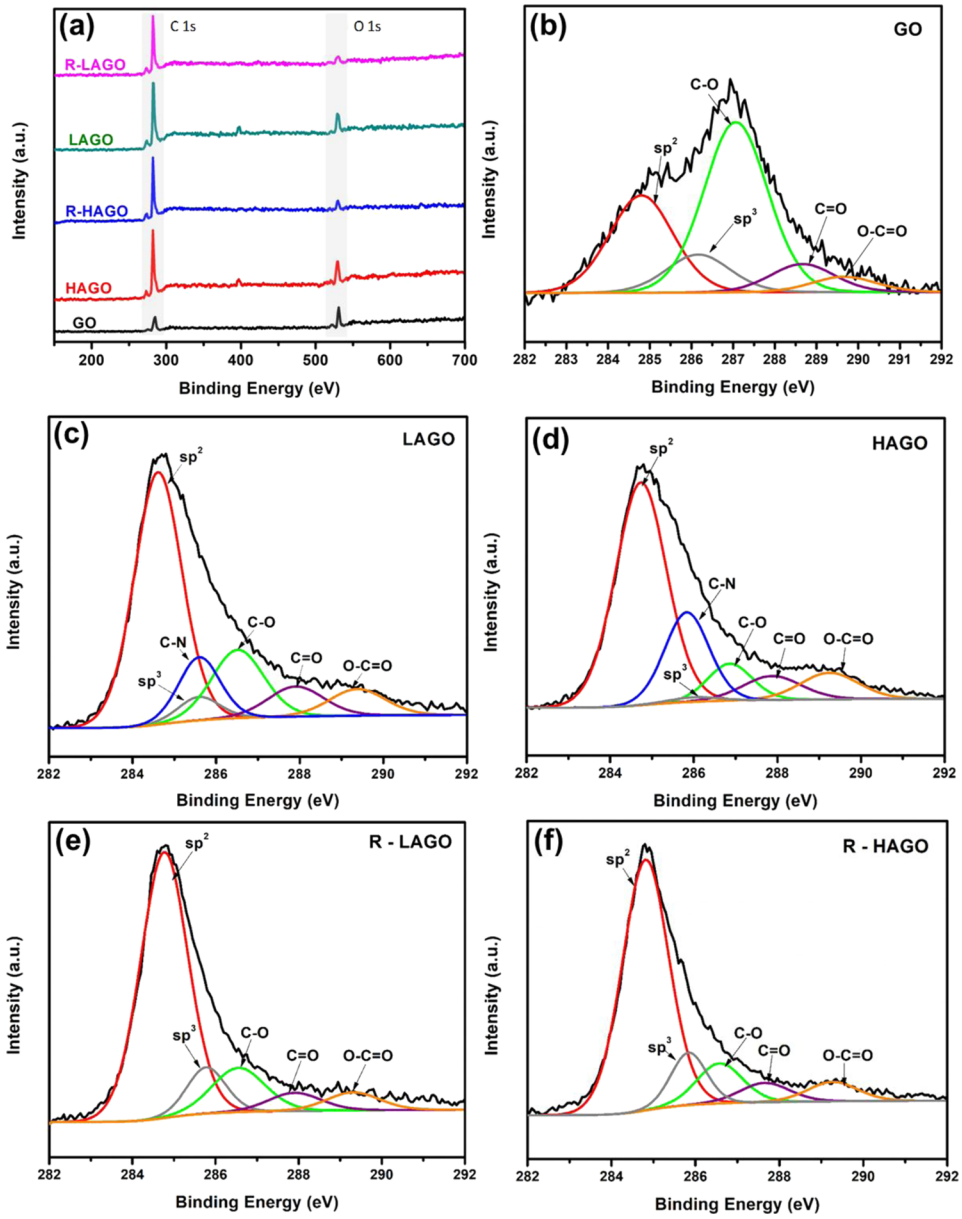

Figure 5. (a) Survey spectra of all aerogels and precursor GO nanosheets. C 1s XPS spectra of (b) precursor GO nanosheets, LAGO and HAGO aerogels (c,d) before and after (e,f) reduction.

Table 1. Atomic Ratio of LAGO and HAGO Aerogels before and after Reduction

	atomic composition (%)		
sample	carbon	oxygen	nitrogen
GO powder	70.0	30.0	0.0
LAGO	81.0	13.2	5.8
R-LAGO	91.5	7.5	1.0
HAGO	72.5	17.3	10.2
R-HAGO	91.5	7.5	1.0

Table 2. Properties of GO Aerogels Prepared at LAGO and HAGO Ratios[a]

properties	LAGO	HAGO
density (g/cm^3) pre-reduction	0.071	0.039
BET surface area (m^2/g) pre-reduction	970	1700
conductivity (S/m) pre-reduction	0.020	0.027
conductivity (S/m) post-reduction	160	560

[a]Note: the standard deviation for these electrical conductivity measurements is 4.7%.

Electrochemical Energy Storage. These gels have potential applications in electrochemical energy storage because of their low density, high surface area, and electrical conductivity; here, we focus on the hydrogel state rather than the dried aerogels as the sample is exposed to the electrolyte. HAGO was selected for investigation because it bore the highest surface area and conductivity. As shown in Figure 6, CV curves were collected on a symmetric supercapacitor cell assembly with pressed HAGO hydrogels as electrodes, platinum current collectors, Celgard separator, and 1 M H_2SO_4 as an electrolyte. The areal capacitance at the scan rate of 2 mV/s, for an ~100 μm thick electrode was calculated to be 463 mF/cm^2, which is comparable to the values reported in a recent study based on supercapacitors made from reduced

DOI: 10.1021/acs.langmuir.8b00637
Langmuir 2018, 34, 8550−8559

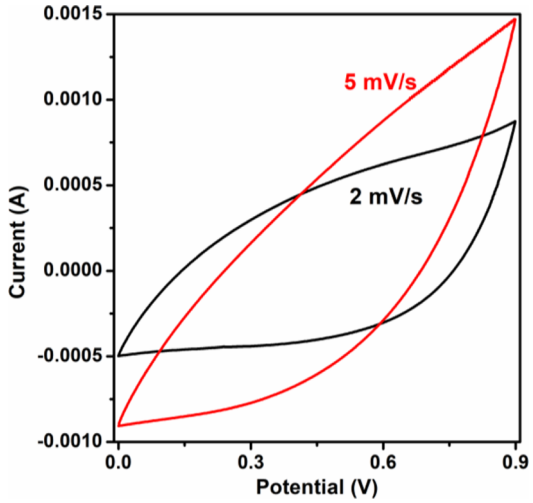

Figure 6. Cyclic voltammogram of the pressed HAGO hydrogel-based supercapacitor at scan rates of 2 and 5 mV/s.

GO gel electrodes.[44] However, at increasing scan rates, this number drops substantially (Supporting Information section S6), indicating that additional reduction may be required to improve the electrical conductivity of these gels. Note that the thermal reduction can only be carried out in the dry state, so wet-state methods for reduction are needed.[45,46]

These data indicate that composition and processing (ammonia/GO ratio) influence a number of properties in the resulting aerogel, including specific surface area, pore size distribution, atomic composition, and morphology. The degree of reduction (during gelation or during subsequent processing) is the dominant parameter affecting the gel's electrical conductivity (and specific capacitance) and may be the limiting factor for many GO gel applications.

GO Morphology Effects. In addition to the ammonia/GO ratio, we also assessed the effects of the parent GO morphology on the morphology of the product gel. Prior studies have indicated that the nanosheet aspect ratio strongly affects the structure of the 3D network, with larger nanosheets interacting at lower concentrations;[47,48] from this perspective, crumpled nanosheets effectively behave like "spherical graphene" with an aspect ratio of 1. We next assess the structure of gels made from such cGO. Initially, the parent cGO particles sprayed at 150 °C were used to synthesize the cGO hydrogels. These particles formed a very brittle hydrogel. The crumpled morphology of the particles and the low density of the bridging structures can be observed in the SEM images of its corresponding aerogel (Supporting Information section S7). The crumpled particles are less prone to $\pi-\pi$ stacking because of their highly wrinkled surface; thus, the physical cross-linking because of the $\pi-\pi$ interactions cannot be the primary mechanism of intersheet cross-linking. In this case, the hydrogel formation relies on the covalent bond formation between the nanosheets. On the other hand, the covalent bond formation requires a sufficient number of functional groups on the GO surface. The spray-drying of the GO sheets at 150 °C may partially remove the functional groups; hence, the covalent bond formation is also hindered in this sample. To study the role of surface functional groups on the parent cGO and verify the covalent bond formation mechanism, we reduced the spraying temperature from 150 to 120 °C to preserve the functional groups on the cGO surface. With increased functional groups on the cGO surface, these cGO particles formed a well-integrated hydrogel with higher density of the bridging structures (Figure 7). Again, an increase in bridging structures is correlated with an increase in functional groups on cGO.

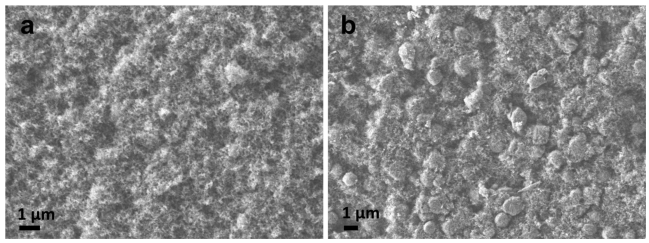

Figure 7. SEM images of cGO aerogels prepared with a (a) 0.024 ammonia/cGO ratio and (b) 0.012 ammonia/cGO ratio. The cGO particles were collected from GO dispersions spray-dried at 120 °C.

Additionally, the cGO aerogels have only sub-micrometer-sized pores, resulting in a higher packing density compared to the GO aerogels. Moreover, the cGO aerogels prepared with low and high ammonia/cGO ratios (0.012 and 0.024, respectively) have densities of 0.067 and 0.072 g/cm^3, which are both closer to that of LAGO than HAGO (Table 3). This may be because cGO particles tend to interact at shorter distances such that higher (denser) packing is required for the same particle−particle interactions and bond formation during gelation. As expected, a higher ammonia/cGO (HAcGO) ratio yields an aerogel with a higher surface area.

To better understand the precursor morphology effect, we also synthesized hydrogels with varying ratios of cGO/GO. At lower cGO/GO ratios, the porous structure roughly resembles that of GO aerogels. The gradual alteration of the aerogels morphology is indicated in Figure 8. This trend of morphological changes with the cGO/GO ratio confirms that the precursor morphology affects the cross-linking mechanism, gel density, and the pore size distribution.

The electrical conductivity and BET surface area of the cGO/GO aerogels are indicated in Table 3. All the aerogels are electrically conductive, and their conductivity values range from ~10^{-3} to 10^{-2} S/m. The electrical conductivity of HAcGO (25% cGO) was found to be higher than that of HAGO samples. This could be attributed to cGO being arranged inside the pores formed by the native (uncrumpled) sheets in HAcGO (25% cGO) aerogels, leading to an increase in density (from HAGO's 0.039 g/cm^3 to 0.069 gm/cm^3) and improved electrical conductivity. In contrast, HAcGO (100% cGO) samples have significantly lower electrical conductivity compared to other aerogel structures because the spherical cGO shape leads to minimal $\pi-\pi$ stacking among adjacent nanosheets. Both GO (Table 2) and cGO aerogels prepared with a higher NH_4OH/nanosheet ratio (v/w) of 0.024 mL/mg displayed higher surface areas than the mixed cGO/GO aerogels. This may be caused by cGO disrupting the native GO nanosheet mechanism of gel formation and preventing the bridging structures from forming.

CONCLUSIONS

In this study, we extensively studied the gelation process of GO for a graphene 3D network with ammonia at low temperature. The morphology and properties of the product gel are determined by the GO/ammonia ratio, the morphology, and

DOI: 10.1021/acs.langmuir.8b00637
Langmuir 2018, 34, 8550−8559

Table 3. Table Summarizing the Properties of cGO and Combined GO/cGO Aerogels[a]

properties	LAcGO[b]	HAcGO	HAcGO (25% cGO)	HAcGO (50% cGO)	HAcGO (75% cGO)
density (g/cm^3) prereduction	0.067	0.072	0.069	0.061	0.160
BET surface area (m^2/g) pre-reduction		1570	1180	1290	998
conductivity (S/m) prereduction	0.012	0.008	0.075	0.031	0.026
conductivity (S/m) postreduction	130	170	140		94

[a]Note: the standard deviation for electrical conductivity measurements is 4.7%. [b]Low ammonia/cGO gel.

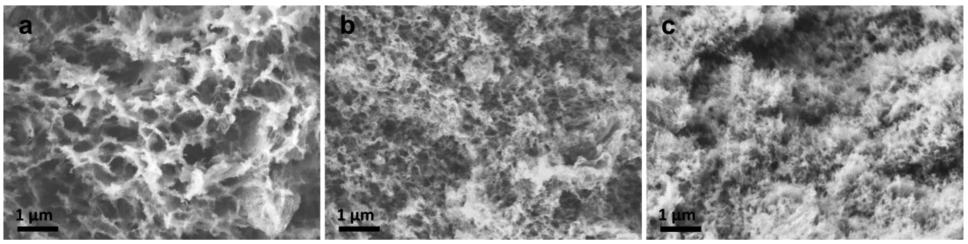

Figure 8. SEM images of 1 wt % aerogels prepared using cGO/GO ratios of (a) 25/75 (b) 50/50, and (c) 75/25. All the cGO particles were sprayed at 120 °C and 40 psi.

surface properties of the parent GO. Bridging structures were observed in samples prepared with a higher ammonia/GO ratio. These structures may be the product of intersheet covalent bonding and thus represent the chemical cross-links in the GO aerogel. Further spectroscopic characterizations are required to reveal the chemical composition of the bridging structure. All the aerogels have reasonable electrical conductivity, which improves significantly after thermal annealing. Moreover, an exceptionally high surface area was observed in aerogels with more bridging cross-links. These characteristics of electrical conductivity and high surface area are critically important for the development of graphene gel-based electrodes for energy storage applications.

We also demonstrated that it is possible to alter the GO nanosheet morphology to a crumpled cGO structure and then prepare cGO aerogels. These aerogels display extensive bridging between the nanosheets; we can infer that the gelation of cGO particles occurs mainly through chemical cross-linking as these particles are less prone to $\pi-\pi$ stacking. This is the first demonstration of cGO as a reaction feedstock for bulk graphene 3D materials.

■ ASSOCIATED CONTENT

Supporting Information

The Supporting Information is available free of charge on the ACS Publications website at DOI: 10.1021/acs.langmuir.8b00637.

EDS mapping of aerogels, SEM of thermally annealed aerogels, N 1s XPS spectra of aerogels, TGA of GO nanosheets and aerogels, specific capacitance dependence on scan rate, and SEM of cGO spray-dried at different temperatures (PDF)

■ AUTHOR INFORMATION

Corresponding Author

*E-mail: micah.green@tamu.edu.

ORCID

Jodie L. Lutkenhaus: 0000-0002-2613-6016

Micah J. Green: 0000-0001-5691-0861

Present Address

[§]Department of Chemical Engineering, MIT, Cambridge, MA 02139.

Author Contributions

D.P., S.S., M.O., and W.S. carried out the experiments. D.P., S.S., and M.J.G. conceived the experimental design. D.P., S.S., J.L., and M.J.G. wrote the paper.

Notes

The authors declare no competing financial interest.

The data sets generated during and/or analyzed during the current study are available from the corresponding author on reasonable request.

■ ACKNOWLEDGMENTS

Funding for this work was provided by the Air Force Office of Scientific Research grant no. FA9550-16-1-0230 and by the U.S. National Science Foundation CAREER award no. CMMI-1253085. We acknowledge Professors Jaime Grunlan and Y. A. Elabd for their helpful comments as well as helpful input in the lab from Linnea Sill. We acknowledge the use of TAMU Materials Characterization Facility. We thank Dr. Venkata Vasiraju in Dr. Sreeram Vaddiraju's group for help with FTIR measurements. We also thank Moonjoo Lee in Dr. Hae-Kwon Jeong's group for help with BET measurements.

■ REFERENCES

(1) Jiang, D.-e.; Cooper, V. R.; Dai, S. Porous graphene as the ultimate membrane for gas separation. *Nano Lett.* **2009**, *9*, 4019−4024.

(2) Ma, Y.; Chen, Y. Three-dimensional graphene networks: synthesis, properties and applications. *Natl. Sci. Rev.* **2015**, *2*, 40−53.

(3) Biener, J.; Stadermann, M.; Suss, M.; Worsley, M. A.; Biener, M. M.; Rose, K. A.; Baumann, T. F. Advanced carbon aerogels for energy applications. *Energy Environ. Sci.* **2011**, *4*, 656−667.

(4) Lei, Z.; Lu, L.; Zhao, X. S. The electrocapacitive properties of graphene oxide reduced by urea. *Energy Environ. Sci.* **2012**, *5*, 6391−6399.

(5) Liu, Y.; Xie, B.; Zhang, Z.; Zheng, Q.; Xu, Z. Mechanical properties of graphene papers. *J. Mech. Phys. Solids* **2012**, *60*, 591−605.

(6) Wu, Z.-S.; Winter, A.; Chen, L.; Sun, Y.; Turchanin, A.; Feng, X.; Müllen, K. Three-Dimensional Nitrogen and Boron Co-doped

DOI: 10.1021/acs.langmuir.8b00637
Langmuir 2018, 34, 8550−8559

Graphene for High-Performance All-Solid-State Supercapacitors. *Adv. Mater.* **2012**, *24*, 5130−5135.
(7) Chen, Z.; Ren, W.; Gao, L.; Liu, B.; Pei, S.; Cheng, H.-M. Three-dimensional flexible and conductive interconnected graphene networks grown by chemical vapour deposition. *Nat. Mater.* **2011**, *10*, 424−428.
(8) Yang, Z.-Y.; Jin, L.-J.; Lu, G.-Q.; Xiao, Q.-Q.; Zhang, Y.-X.; Jing, L.; Zhang, X.-X.; Yan, Y.-M.; Sun, K.-N. Sponge-Templated Preparation of High Surface Area Graphene with Ultrahigh Capacitive Deionization Performance. *Adv. Funct. Mater.* **2014**, *24*, 3917−3925.
(9) Qiu, L.; Liu, J. Z.; Chang, S. L. Y.; Wu, Y.; Li, D. Biomimetic superelastic graphene-based cellular monoliths. *Nat. Commun.* **2012**, *3*, 1−7.
(10) Cao, X.; Shi, Y.; Shi, W.; Lu, G.; Huang, X.; Yan, Q.; Zhang, Q.; Zhang, H. Preparation of novel 3D graphene networks for supercapacitor applications. *Small* **2011**, *7*, 3163−3168.
(11) Niu, Z.; Liu, L.; Zhang, L.; Shao, Q.; Zhou, W.; Chen, X.; Xie, S. A Universal Strategy to Prepare Functional Porous Graphene Hybrid Architectures. *Adv. Mater.* **2014**, *26*, 3681−3687.
(12) Cong, H.-P.; Ren, X.-C.; Wang, P.; Yu, S.-H. Macroscopic Multifunctional Graphene-Based Hydrogels and Aerogels by a Metal Ion Induced Self-Assembly Process. *ACS Nano* **2012**, *6*, 2693−2703.
(13) Bai, H.; Li, C.; Wang, X.; Shi, G. On the gelation of graphene oxide. *J. Phys. Chem. C* **2011**, *115*, 5545−5551.
(14) Bai, H.; Li, C.; Wang, X.; Shi, G. A pH-sensitive graphene oxide composite hydrogel. *Chem. Commun.* **2010**, *46*, 2376−2378.
(15) Huang, C.; Bai, H.; Li, C.; Shi, G. A graphene oxide/hemoglobin composite hydrogel for enzymatic catalysis in organic solvents. *Chem. Commun.* **2011**, *47*, 4962−4964.
(16) Bai, H.; Sheng, K.; Zhang, P.; Li, C.; Shi, G. Graphene oxide/conducting polymer composite hydrogels. *J. Mater. Chem.* **2011**, *21*, 18653−18658.
(17) Ai, W.; Du, Z.-Z.; Liu, J.-Q.; Zhao, F.; Yi, M.-D.; Xie, L.-H.; Shi, N.-E.; Ma, Y.-W.; Qian, Y.; Fan, Q.-L.; Yu, T.; Huang, W. Formation of graphene oxide gel via the π-stacked supramolecular self-assembly. *RSC Adv.* **2012**, *2*, 12204−12209.
(18) Worsley, M. A.; Pauzauskie, P. J.; Olson, T. Y.; Biener, J.; Satcher, J. H., Jr.; Baumann, T. F. Synthesis of Graphene Aerogel with High Electrical Conductivity. *J. Am. Chem. Soc.* **2010**, *132*, 14067−14069.
(19) Xu, Y.; Sheng, K.; Li, C.; Shi, G. Self-Assembled Graphene Hydrogel via a One-Step Hydrothermal Process. *ACS Nano* **2010**, *4*, 4324−4330.
(20) Bai, H.; Li, C.; Wang, X.; Shi, G. On the Gelation of Graphene Oxide. *J. Phys. Chem. C* **2011**, *115*, 5545−5551.
(21) Wang, J.; Ellsworth, M. Graphene aerogels. *ECS Trans.* **2009**, *19*, 241−247.
(22) Worsley, M. A.; Kucheyev, S. O.; Mason, H. E.; Merrill, M. D.; Mayer, B. P.; Lewicki, J.; Valdez, C. A.; Suss, M. E.; Stadermann, M.; Pauzauskie, P. J.; Satcher, J. H.; Biener, J.; Baumann, T. F. Mechanically robust 3D graphene macroassembly with high surface area. *Chem. Commun.* **2012**, *48*, 8428−8430.
(23) Irin, F.; Das, S.; Atore, F. O.; Green, M. J. Ultralow Percolation Threshold in Aerogel and Cryogel Templated Composites. *Langmuir* **2013**, *29*, 11449−11456.
(24) Worsley, M. A.; Charnvanichborikarn, S.; Montalvo, E.; Shin, S. J.; Tylski, E. D.; Lewicki, J. P.; Nelson, A. J.; Satcher, J. H.; Biener, J.; Baumann, T. F.; Kucheyev, S. O. Toward Macroscale, Isotropic Carbons with Graphene-Sheet-Like Electrical and Mechanical Properties. *Adv. Funct. Mater.* **2014**, *24*, 4259−4264.
(25) Hu, K.; Xie, X.; Szkopek, T.; Cerruti, M. Understanding Hydrothermally Reduced Graphene Oxide Hydrogels: From Reaction Products to Hydrogel Properties. *Chem. Mater.* **2016**, *28*, 1756−1768.
(26) Han, Z.; Tang, Z.; Li, P.; Yang, G.; Zheng, Q.; Yang, J. Ammonia solution strengthened three-dimensional macro-porous graphene aerogel. *Nanoscale* **2013**, *5*, 5462−5467.
(27) Luo, J.; Jang, H. D.; Sun, T.; Xiao, L.; He, Z.; Katsoulidis, A. P.; Kanatzidis, M. G.; Gibson, J. M.; Huang, J. Compression and aggregation-resistant particles of crumpled soft sheets. *ACS Nano* **2011**, *5*, 8943−8949.
(28) Parviz, D.; Metzler, S. D.; Das, S.; Irin, F.; Green, M. J. Tailored Crumpling and Unfolding of Spray-Dried Pristine Graphene and Graphene Oxide Sheets. *Small* **2015**, *11*, 2661−2668.
(29) Kovtyukhova, N. I.; Ollivier, P. J.; Martin, B. R.; Mallouk, T. E.; Chizhik, S. A.; Buzaneva, E. V.; Gorchinskiy, A. D. Layer-by-Layer Assembly of Ultrathin Composite Films from Micron-Sized Graphite Oxide Sheets and Polycations. *Chem. Mater.* **1999**, *11*, 771−778.
(30) Dimiev, A.; Kosynkin, D. V.; Alemany, L. B.; Chaguine, P.; Tour, J. M. Pristine Graphite Oxide. *J. Am. Chem. Soc.* **2012**, *134*, 2815−2822.
(31) Goldstein, A. P.; Mickelson, W.; Machness, A.; Lee, G.; Worsley, M. A.; Woo, L.; Zettl, A. Simultaneous Sheet Cross-Linking and Deoxygenation in the Graphene Oxide Sol−Gel Transition. *J. Phys. Chem. C* **2014**, *118*, 28855−28860.
(32) Lv, W.; Zhang, C.; Li, Z.; Yang, Q.-H. Self-Assembled 3D Graphene Monolith from Solution. *J. Phys. Chem. Lett.* **2015**, *6*, 658−668.
(33) Rourke, J. P.; Pandey, P. A.; Moore, J. J.; Bates, M.; Kinloch, I. A.; Young, R. J.; Wilson, N. R. The Real Graphene Oxide Revealed: Stripping the Oxidative Debris from the Graphene-like Sheets. *Angew. Chem., Int. Ed.* **2011**, *50*, 3173−3177.
(34) Dreyer, D. R.; Todd, A. D.; Bielawski, C. W. Harnessing the chemistry of graphene oxide. *Chem. Soc. Rev.* **2014**, *43*, 5288−5301.
(35) Thomas, H. R.; Day, S. P.; Woodruff, W. E.; Vallés, C.; Young, R. J.; Kinloch, I. A.; Morley, G. W.; Hanna, J. V.; Wilson, N. R.; Rourke, J. P. Deoxygenation of Graphene Oxide: Reduction or Cleaning? *Chem. Mater.* **2013**, *25*, 3580−3588.
(36) Pan, S.; Aksay, I. A. Factors Controlling the Size of Graphene Oxide Sheets Produced via the Graphite Oxide Route. *ACS Nano* **2011**, *5*, 4073−4083.
(37) Kudo, A.; Campbell, P. G.; Biener, J. Nanographene Aerogels: Size Effect of the Precursor Graphene Oxide on Gelation Process and Electrochemical Properties. *ChemNanoMat* **2018**, *4*, 338−342.
(38) Kim, H. J.; Lee, S.-M.; Oh, Y.-S.; Yang, Y.-H.; Lim, Y. S.; Yoon, D. H.; Lee, C.; Kim, J.-Y.; Ruoff, R. S. Unoxidized Graphene/Alumina Nanocomposite: Fracture- and Wear-Resistance Effects of Graphene on Alumina Matrix. *Sci. Rep.* **2014**, *4*, 5176.
(39) Yang, D.; Velamakanni, A.; Bozoklu, G.; Park, S.; Stoller, M.; Piner, R. D.; Stankovich, S.; Jung, I.; Field, D. A.; Ventrice, C. A.; Ruoff, R. S. Chemical analysis of graphene oxide films after heat and chemical treatments by X-ray photoelectron and Micro-Raman spectroscopy. *Carbon* **2009**, *47*, 145−152.
(40) Wang, G.; Jia, L.-T.; Zhu, Y.; Hou, B.; Li, D.-B.; Sun, Y.-H. Novel preparation of nitrogen-doped graphene in various forms with aqueous ammonia under mild conditions. *RSC Adv.* **2012**, *2*, 11249−11252.
(41) Chen, L.-F.; Huang, Z.-H.; Liang, H.-W.; Yao, W.-T.; Yu, Z.-Y.; Yu, S.-H. Flexible all-solid-state high-power supercapacitor fabricated with nitrogen-doped carbon nanofiber electrode material derived from bacterial cellulose. *Energy Environ. Sci.* **2013**, *6*, 3331−3338.
(42) Yang, S.; Zhi, L.; Tang, K.; Feng, X.; Maier, J.; Müllen, K. Efficient Synthesis of Heteroatom (N or S)-Doped Graphene Based on Ultrathin Graphene Oxide-Porous Silica Sheets for Oxygen Reduction Reactions. *Adv. Funct. Mater.* **2012**, *22*, 3634−3640.
(43) Lin, Z.; Waller, G.; Liu, Y.; Liu, M.; Wong, C.-P. Facile Synthesis of Nitrogen-Doped Graphene via Pyrolysis of Graphene Oxide and Urea, and its Electrocatalytic Activity toward the Oxygen-Reduction Reaction. *Adv. Energy Mater.* **2012**, *2*, 884−888.
(44) Xu, Y.; Lin, Z.; Huang, X.; Liu, Y.; Huang, Y.; Duan, X. Flexible Solid-State Supercapacitors Based on Three-Dimensional Graphene Hydrogel Films. *ACS Nano* **2013**, *7*, 4042−4049.
(45) Zhang, J.; Yang, H.; Shen, G.; Cheng, P.; Zhang, J.; Guo, S. Reduction of graphene oxide vial-ascorbic acid. *Chem. Commun.* **2010**, *46*, 1112−1114.
(46) Fernández-Merino, M. J.; Guardia, L.; Paredes, J. I.; Villar-Rodil, S.; Solís-Fernández, P.; Martínez-Alonso, A.; Tascón, J. M. D. Vitamin C Is an Ideal Substitute for Hydrazine in the Reduction of

DOI: 10.1021/acs.langmuir.8b00637
Langmuir 2018, 34, 8550−8559

Graphene Oxide Suspensions. *J. Phys. Chem. C* **2010**, *114*, 6426−6432.
(47) Ruzicka, B.; Zaccarelli, E. A fresh look at the Laponite phase diagram. *Soft Matter* **2011**, *7*, 1268−1286.
(48) Wu, Q.; Meng, Y.; Wang, S.; Li, Y.; Fu, S.; Ma, L.; Harper, D. Rheological Behavior of Cellulose Nanocrystal Suspension: Influence of Concentration and Aspect Ratio. *J. Appl. Polym. Sci.* **2014**, *131*, 40525.

DOI: 10.1021/acs.langmuir.8b00637
Langmuir 2018, 34, 8550−8559